J Mater Sci: Mater Electron (2021) 32:26984–26997

Effect of Ni-doping on the structural, magnetic, and electronic properties of $La_{0.2}Sr_{0.8}MnO_3$ perovskite

Nejeh Hamdaoui[1,*], Dhahbi Tlili[2], Yashar Azizian-Kalandaragh[3,4], Boubaker Zaidi[5,6], Sadok Zemni[2], Alaa Ahmed Akl[6,7], and Lotfi Beji[8]

[1] *ISITCom, University of Sousse, Gp1, 4011 Hammam Sousse, Tunisia*
[2] *Laboratory of Physical Chemistry of Materials, Department of Physics, Faculty of Science of Monastir, University of Monastir, Monastir, Tunisia*
[3] *Department of Physics, University of Mohaghegh Ardabili, P.O. Box.179, Ardabil, Iran*
[4] *Department of Photonics, Faculty of Applied Sciences, Gazi University, Ankara, Turkey*
[5] *Laboratoire Physico-Chimie des Matériaux, Département de Physique, Faculté des Sciences de Monastir, Université de Monastir, 5000 Monastir, Tunisia*
[6] *Physics Department, Faculty of Science and Humanities in Ad-Dawadmi, Shaqra University, Shaqra 11911, Saudi Arabia*
[7] *Physics Department, Faculty of Sciences, Minia University, Minia 61519, Egypt*
[8] *Departement of Physics, College of Sciences and Arts at Ar Rass, Qassim University, Ar Rass, Saudi Arabia*

Received: 21 June 2021
Accepted: 19 September 2021
Published online: 25 September 2021

ABSTRACT

The effect of light Ni-substituted Manganese on the physical properties of $La_{0.2}Sr_{0.8}MnO_3$ perovskite prepared by the standard solid-state reaction method was investigated. Field Emission Scanning Electron microscopy confirms the particle size composition and grain boundaries in these samples. Moreover, the presence of all the chemical elements with atomic ratios coordinating with the general formula $La_{0.2}Sr_{0.8}Mn_{1-x}Ni_xO_3$ ($x = 0.0$ and 0.1) was confirmed by Energy-dispersive X-ray spectroscopy. X-ray diffractions analyses indicate that both compounds have a rhombohedral structure with an R3C space group, for which the cell parameter increases with nickel addition. A competition between ferromagnetic and antiferromagnetic moments is evidenced at room temperature for both compounds by measuring the magnetization versus magnetic field. Saturation magnetization and the corresponding residual magnetization decrease with the Ni substitution; however, the coercive field increases. These changes are correlated with those evidenced by structural properties. Conductance measurements as a function of frequency from 10^2 Hz to 5 MHz are analyzed in the temperature range 300 K–420 K in order to evidence the conduction mechanism.

Address correspondence to E-mail: hamdaoui_nejeh@protonmail.com; hamdaoui_nejeh@yahoo.fr

https://doi.org/10.1007/s10854-021-07072-1

1 Introduction

Due to their variety of applications, manganite perovskites materials are recently devoted with continuous structural, magnetic, and electronic investigations. These materials exhibit various electric and magnetic phenomena depending on the composition of each element, such as ferromagnetic, antiferromagnetic, charge, and orbital ordering [1]. The properties of these materials are principally derived from the double-exchange interaction Mn^{3+}–O–Mn^{4+} [2]. Consequently, they can drive excellent magneto-transport properties, based on both ferromagnetic and antiferromagnetic complexes allowing their use as active layer in spintronics devices [3] and sensors [4]. Indeed, the discovery of colossal magneto-resistance (CMR) [5] in these manganites represents a starting point for benefitting technological applications such as sensors for magnetometry applications [6], storage media [7], and supercapacitors [8]. These exotic applications are based on the competition between spin and freedom lattice degree [9].

Among these manganites, $SrMnO_3$ perovskite has been used as active layers for humidity monitoring applications due to its low cost, low contamination impact, and good stability of the resistivity and environmental factors [10]. The $SrMnO_3$ has been also extended for super-capacitor prototype with higher cycling stability [8]. Moreover, a combination of optoelectronic, magnetic, and thermoelectric study with DFT calculations supports its applications for UV visible optical devices [11].

Scientific communities try continuously to understand the mechanism in manganite materials formation in order to improve their properties which can lead to their use in specific applications. Consequently, much attention has been devoted to explain the fundamental mechanisms combining their magnetic and transport properties. To improve physical functionalities, we often proceed by a substitution ABO_3 in A or B sites with a series of alkaline earth or rare earth metal ions. Particularly, the substitution induces change in the Curie temperature and saturation magnetization [12], due to the fact that the rare earth substitution leads to a change of valence states of manganese which plays a core role in the transport properties. The quaternary $La_{1-x}Sr_xMnO_3$ has been classified among the materials with excellent CMR effects. The increase of the Sr concentration more than 0.5 leads to some change due to the straightness of the bonds Mn–O–Mn [9]. The ferromagnetism of these materials is essentially derived from structural properties such as oxygen vacancies [13], double-exchange interaction $Mn^{3+/}Mn^{4+}$, and the strain. Moreover, the simple substitution of Ni in Mn site of $La_{0.8}Sr_{0.2}MnO_3$ is an efficient way to tune its bifunctional catalytic activity [14]. Added to the higher relative cooling power (RCP), it has been demonstrated that the transition temperature and MCE are tuned to nearly room temperature by Ni substitution for Ni concentration of 0.1 [15, 16].

Recent progress are nowadays focused on the rare earth element substitution on perovskite manganite at the nano-scale, exhibiting new experimental behaviors which can be used for new nano-electronic devices [10]. In this work, we are interested in the nickel-substituted manganese on the perovskite oxides $La_{0.2}Sr_{0.8}MnO_3$ at lower Ni concentration prepared with the standard solid-state reaction method. Changes of structural properties have been studied by X-ray diffraction (XRD) analyses and field emission scanning electron microscope (FESEM) coupled with energy-dispersive X-ray (EDX) analysis. Then, in order to evaluate the effect of manganese substitution on the magnetic properties, magnetization has been measured using vibrating sample magnetometer. Moreover, conductance measurements are analyzed in large frequential domain (10^2 Hz–5 MHz) in order to evidence the effect of Ni-substituted Mn on the conduction mechanism.

2 Experimental details

Perovskite oxides $La_{0.2}Sr_{0.8}MnO_3$ (LSMO) and $La_{0.2}Sr_{0.8}Mn_{0.9}Ni_{0.1}O_3$ (LSMNO) powders were prepared by the standard solid-state reaction method [16]. The precursors LaO_3, SrO_3, MnO_3, and NiO with purity better than 99.99% were weighed with the stoichiometric ratios and mixed using an agate mortar and then calcined at 1000 °C for 8 h. The resulting powders were ground, pelletized, and sintered at 1500 °C for 48 h with one intermediate grinding. The powders of both samples, thus, obtained were well ground again and were compressed into pellets of 8 mm (1 mm) diameter (thickness). On the other hand, in order to decrease their porosities, both materials were annealed at 1500 °C for 24 h under oxygen atmosphere.

The structural properties are studied using a Philips X pert, X-ray diffractometer with CuKα radiation (λ = 1.54 Å). FESEM is employed to examine the morphological characteristics of the samples and also EDX analysis was used to check the presence of chemical elements introduced during the sample preparation using a FESEM, TeScan—Mira III, Czech Republic. A vibrating sample magnetometer (8600 Series VSM Model lake shore) was employed to study the magnetic properties of both samples at room temperature. Conductance measurement data are deduced from impedance spectroscopy measurements using an N4L-NumetriQ type PSM1735.

3 Results and discussion

3.1 X-ray diffraction results

Figure 1 shows XRD patterns of both samples LSMO and LSMNO. In both cases, the interplanar lines spacing was calculated in order to investigate the phase formation and probe the structure of the synthesized $La_{0.2}Sr_{0.8}Mn_{1-x}Ni_xO_3$. As shown, XRD pattern of both samples reveals that a pure and single-phase perovskite structure has been successfully formed. No trace of the secondary phase was detected within the sensitivity limit of the experiment. All the patterns are in good accordance with the JCPDS card no. 01-075-0440 as shown in Table 1. It is concluded that the lines in the pattern's major planes (012), (020), (110), (202), (024), (116), (214), (208), (006), and (128) indicate rhombohedral (hexagonal setting) perovskite structure with space group R3C. As shown in Table 1, no additional lines are detected after nickel addition, reflecting that both materials exhibit the same phase.

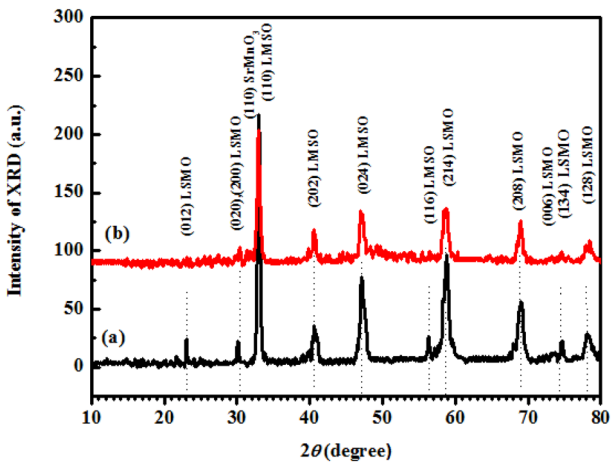

Fig. 1 X-ray diffraction pattern of polycrystalline LSMO (**a**) and LSMNO (**b**) fired at 1500 °C in air for 24 h, showing the Miller index of the corresponding plans

The average of lattice parameters was calculated for all lines in each sample according to the following formula [17, 18]:

$$\frac{1}{d_{hkl}^2} = \frac{4}{3}\left(\frac{h^2 + hk + k^2}{a^2}\right) + \frac{L^2}{c^2} \quad (1)$$

where d_{hkl} is the interplanar spacing (recorded automatically) and h, k, and l are the Miller indices of each plane. The lattice parameters for LSMO sample were $a = b$ = 5.4929 Å and c = 13.3235 Å, while for the LSMNO sample they were $a = b$ = 5.5072 and c = 13.3875 Å which exactly match the value given in this card ($a = b$ = 5.4694 and c = 13.4183 Å). Unit cell volume and lattice parameters increase after Nickel addition as summarized in Table 2 and follow the same trend found by Wang et al. [19] and Kuharuangrong et al. [20]. The nickel ion can be present as Ni^{2+} as the most stable state with radius 0.70 Å. Other states of nickel can also be present such low Ni^{3+} high spin, Ni^{3+} lower spin, and Ni^{4+} with radii, respectively, of 0.56 Å, 0.60 Å, and 0.48 Å. However, as previously reported, Mn ions are likely to be in the Mn^{3+} low spin or Mn^{4+} states with radii of 0.58 Å and 0.53 Å, respectively [21]. However, it has been largely reported in the literature that when substituting Mn by Ni via X-ray Photoelectron spectroscopy (XPS) and/or Electron paramagnetic resonance (EPR) studies Nickel exist as Ni^{2+} ions [14, 19, 22], especially at lower Ni concentration.

Furthermore, as shown in Fig. 2, we show a shift of plane (110) position toward smaller angle, accompanied with a peak broadening and a decrease of the XRD intensity. Similar behavior has been previously reported for $La_{0.7}Sr_{0.3}Mn_{1-x}Cr_xO_3$ [23]. These effects are attributed to the crystallite size growth and/or to the decrease in the degree of crystallinity. The value of integral line breadth (area under the peak/maximum peak intensity) was used to obtain the pure broadening of the characteristic peak for both LSMO and LSMNO perovskites [24]. The integral breadth of observation (B) in the sample is corrected by subtracting the value of the instrumental broadening (b) to give only that of pure sample breadth (β). Figure 3 shows the integral breath of both LSMO and

Table 1 XRD data of major peaks analysis, Millar indices, area under the peak, Bragg's angles, d-values, maximum intensity of X-ray, and the integral breadth of LSMO and LSMNO samples

No	(*hkl*)	LSMO					LSMNO				
		Area	$2\theta_0$	d(Å)	I_{max}	β(rad) × 10^{-3}	Area	$2\theta_0$	d(Å)	I_{max}	β(rad) × 10^{-3}
1	(012)	46.50	23.033	3.862	75	24.15	50.13	23.083	3.853	55	28.86
2	(020), (200)	54.15	30.083	2.971	72	30.18	49.95	30.333	2.947	65	34.94
3	(110)	174.30	32.983	2.716	271	32.40	131.95	32.933	2.720	168	37.20
4	(202)	111.75	40.633	2.221	86	36.86	67.55	40.533	2.226	79	42.00
5	(024)	166.08	47.133	1.928	129	39.72	107.33	46.983	1.934	96	46.48
6	(116)	75.78	56.333	1.633	77	43.53	56.83	56.433	1.631	59	50.34
7	(214)	228.80	58.783	1.571	147	44.47	131.03	58.433	1.579	98	51.30
8	(208)	127.35	69.033	1.360	108	46.06	91.78	68.983	1.362	87	52.90
9	(006)	72.35	74.733	1.270	74	45.44	36.35	74.483	1.274	59	53.87
10	(128)	115.53	78.133	1.223	81	47.66	82.60	78.433	1.219	69	55.14

Table 2 XRD data analysis of LSMO and LSMNO samples prepared at 1500 °C in air for 24 h

Parameters	LSMO	LSMNO
Lattice parameters (Å)	$a = b = 5.493$; $c = 13.324$	$a = b = 5.507$; $c = 13.388$
Volume of unit cell (Å^3)	401.996	406.033
Average integral breadth (β_{Int}) (radian)	5.626×10^{-3}	6.407×10^{-3}
Estimated average crystallite size (D_{Int}) (nm)	26	23
Average micro-strain $< \varepsilon_{Int} >$	4.752×10^{-3}	5.406×10^{-3}
Correction average of FWHM (β_{FWHM}) (radian)	5.072×10^{-3}	5.963×10^{-3}
Estimated average crystallite size (D_{FWHM}) (nm)	29	25
Average micro-strain $< \varepsilon_{FWHM} >$	4.281×10^{-3}	5.034×10^{-3}
Crystalline area of the peaks, (A_C)	657.975	805.475
Total area of the whole pattern $A_T = (A_A + A_C)$	871.65	694.50
Degree of crystallinity $X_C = 100{\cdot}Ac/(A_A + A_C)$	75.49%	50.32%
Amorphous area (A_A)	211.675	345.05
Amorphousity degree, $X_A = 100{\cdot}A_A/(A_A + A_C)$	24.50%	49.68%

LSMNO perovskites. As is evident from the figure, the broadening of the XRD peaks increases with the addition of nickel which may be the consequence of smaller grain sizes [21]. It is noted that the phase of LSMO after adding nickel is not changed, due to the fact that both Ni^{2+}-ion and Mn^{3+}-ion have similar ionic radii (70 pm and 72 pm respectively), giving rise to easier substitution process. The manganite LSMNO exhibits a more large bandwidth reflecting a weak electron and phonon interaction. This weak electron–phonon interaction indicates that lattice effects are minor by comparison to those induced by electronic and magnetic structure modifications. Therefore, Ni^{2+}-ion can only be used as a control parameter to change the magnetic and transport properties of these manganite's [25–29].

The physical, mechanical, and morphological properties of perovskites depend on the degree of crystallinity and on the growth of the preferred orientation in the crystal part. Usually, both quantities depend on the different parameters used on the preparation method, such as the sintering temperature, the heating time, and the cooling rate [30, 31]. The heat treatment of the samples reduces residual stored stress, internal stress, average crystallite sizes, and beak breadths. Thus, perovskite is usually a mixture of the crystalline and amorphous phases [32]. The XRD data were used to calculate the degree of

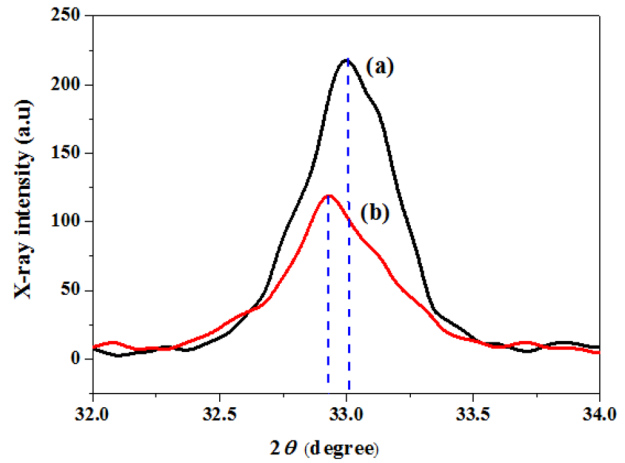

Fig.2 The shift of (110) plane position from LSMO (**a**) to LSMNO (**b**)

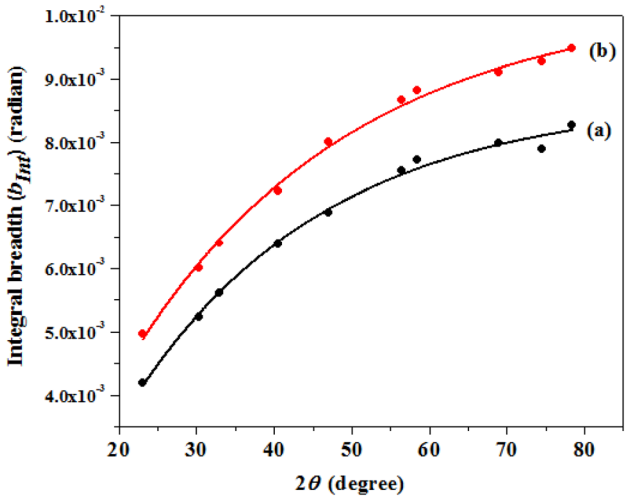

Fig. 3 Integrated breadth of the main planes of the two samples LSMO (**a**) and LSMNO (**b**)

crystallinity of the semi-crystalline perovskite [33–36]. The procedure consists on calculating each of the peaks area corresponding to (012), (020), (110), (202), (024), (116), (214), (208), (006), and (128) planes and by assuming their sum as the crystalline part. The amorphous contribution is, however, estimated by the wide diffraction band of the spectrum, approximated by the background curve. A typical fitting procedure is used in this work to separate the crystalline peaks from the amorphous pattern of LSMO and LSMNO. The crystalline part was separated from the amorphous part by EVA software using the Hermans–Weidinger method [37]. Then, the degree of crystallinity, X_C, was obtained for each sample as a ratio between the area under the crystal peaks, A_C, and the total area under the diffraction curve, $A_T = A_A + A_C$.

$$X_C = \frac{100.A_C}{A_A + A_C} \tag{2}$$

The degree of crystallinity and the degree of Amorphousity are estimated and recorded in Table 2. As it is shown, the amorphousity is increased after Ni addition.

An XRD profile analysis is one of the most accurate techniques for estimating the crystallite size [38–41] and the irregular displacement strain of the atoms with respect to the positions of the reference lattice [42].

The three most important sources of line broadening are the instrumental factor, crystallite size, and micro-strain. The calculation is based on the shape of the peak where there are two ways. Full width at half maximum (FWHM) and integral breadth are applied to the shape of the peaks and leads to more accurate results as in the following relationships [43]:

$$\beta_{hkl} = \beta_L = \beta_{strain} + \beta_{crystallitesize} + \beta_{inst} \tag{3}$$

$$\beta_{correct} = \beta_L = (\beta_{hkl} - \beta_{inst}) = \beta_{strain} + \beta_{crystallitesize} \tag{4}$$

The crystallite size and micro-strain are calculated according to the Debye–Scherrer's relationships [17, 43, 44]:

$$D_{FWHM} = \frac{k\lambda}{\beta_{FWHM}\cos\theta} \text{ and } D_{Int} = \frac{k\lambda}{\beta_{Int}\cos\theta} \tag{5}$$

$$\langle\varepsilon_{FWHM}\rangle = \frac{\beta_{FWHM}\cot\theta}{4} \text{ and } \langle\varepsilon_{Int}\rangle = \frac{\beta_{Int}\cot\theta}{4} \tag{6}$$

In Eq. (6), K is the shape factor taken in our case which is equal to 0.94, since there is not another analysis to estimate the average of crystallites shapes to evaluate its proper value. λ is the incident X-ray wavelength (λ = 0.1542 nm), D is the crystallite size, and $\langle\varepsilon\rangle$ is the average micro-strain. The crystallite size and internal micro-strain were calculated according to the FWHM and integral breadth for both LSMO and LSMNO. All results are summarized in Table 2. It should be noted that the obtained nanocrystallite sizes remains an estimation due to the instrumental limits and the crystallite shape distribution [45]. The estimated average value of nanocrystallite is considered to be decreased as the case of many Ni-substituted Mn in large variety manganites [15, 19, 22, 46, 47]. That is, as the strength of the chemical bonds between the elements decrease, and

consequently, the crystallization decreases. On the other hand, the internal micro-strain exhibited a contrast behavior, i.e., a gradual increase when adding nickel ions is evidenced. This difference may be due to lower degree of preferred direction and lower structural defects including grain boundaries. Because of the high degree of preferred orientation, a single meditation arrangement can be measured with sufficient accuracy.

3.2 Surface morphology and compositional analysis

In order to study the surface morphology of the perovskite samples using a FESEM and estimate the proportions of the elements using EDX, the powder samples were affixed to a glass (SiO_2) holder. So we notice the presence of the characteristic line of the silicon element in the spectrum of the two samples. The microstructure of LSMO and LSMNO obtained by FESEM shows the effect of nickel-substituted Mn on the surface morphology as shown in Fig. 4. Where many microscopic images were photographed at different position and magnifications starting from 10 to 135kx for each sample, and the large magnification was chosen to show the most accurate details of the surface morphology. Figures 4a and b illustrate the FESEM micrographs obtained for LSMO and LSMNO at the same magnification (5kx) to make easier comparison showing a decreasing trend in particle sizes after Ni substitution. The structure shows strong agglomeration of nanoparticles in all samples constituted by grains and grain boundaries. This is evidence of the good growth of the crystallization during the thermal preparation process. It has been confirmed that Ni substitution leads to a decreased particle size of perovskite oxides, as recently reported in the case of $La_{0.7}Sr_{0.3}Mn_{1-x}Ni_xO_3$ [48]. The reduction in particle size leads to an increase in the surface area of the granules specified for perovskite oxide, as LSMNO exhibits a greater surface area of the grains, nearly twice the surface area of the non-activated LSMO. The average particle size in the case of LSMO (180 nm to 270 nm) was strongly reduced for LSMNO (80 to 190 nm) and calculated according to the analysis of several FESEM obtained images [27, 49]. In Fig. 4, images (c) and (d), having the same magnification of 70kx, we notice cracking and demolition in crystal agglomeration and a decrease in particle size after adding nickel. Same effects are also seen for images (e) and (f), which are taken at the same magnification of 135kx. Disintegration, destruction of crystal agglomeration, and reduction of particle size are the most revealed effects with the addition of the Nickel element.

In addition, EDX spectra shown in Fig. 5 reveal the presence of all chemical elements (La, Sr, Ni, Mn and O) that were introduced along the development of LSMO and LSMNO samples, confirming that there

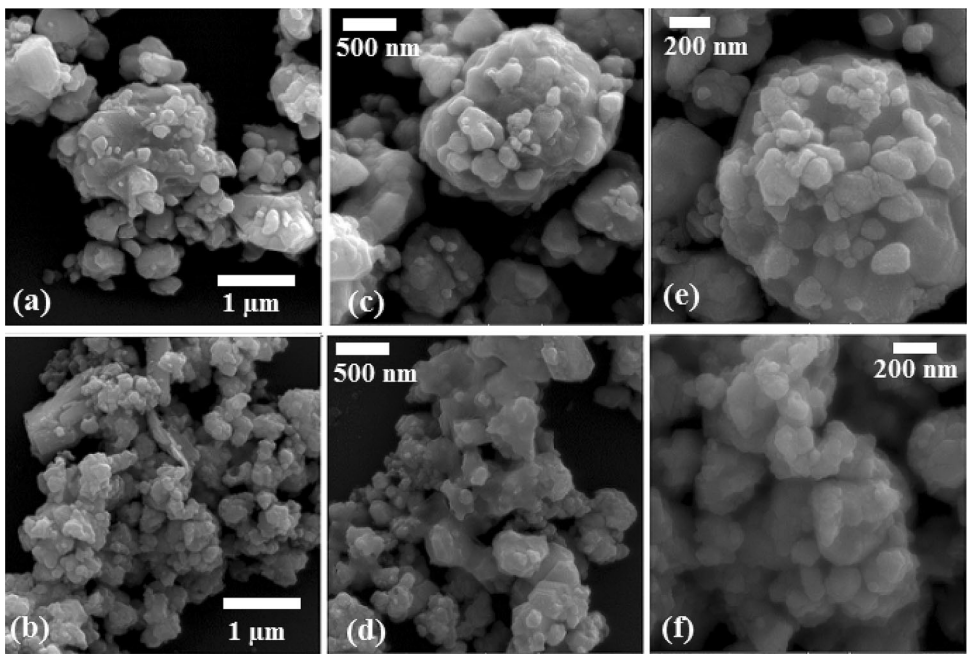

Fig. 4 High-resolution scanning electron microscopy (HRSEM) micrographs of the LSMO (**a**, **c**, **e**) and LSMNO (**b**, **d**, **f**) samples prepared at 1500 °C for 24 h at different magnifications; as the zoom for the two images (**a**) and (**b**) was 50kx, and for the two images (**c**) and (**d**) was 70kx, while the zoom for the two images (**e**) and (**f**) was 135kx

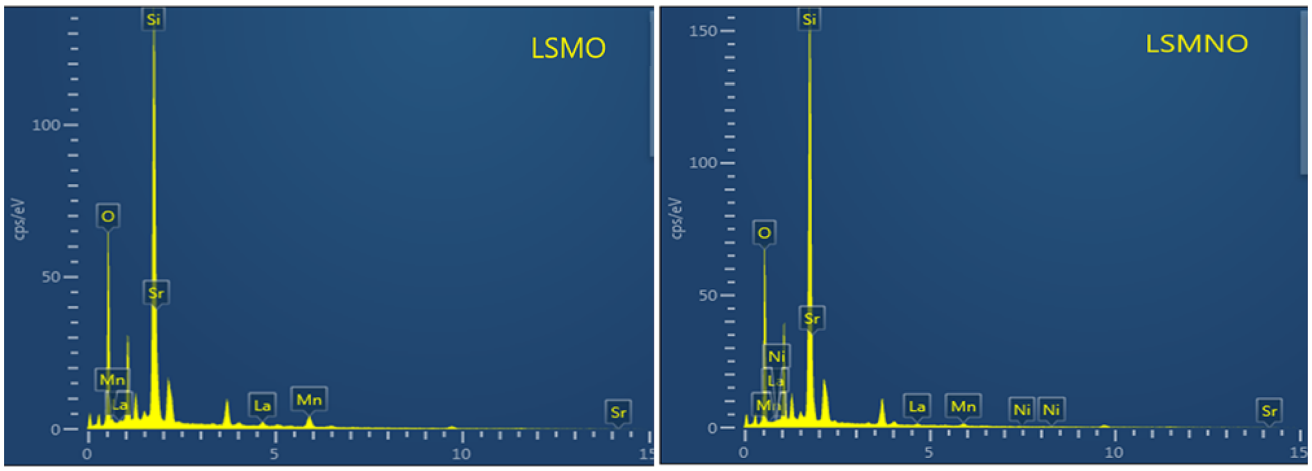

Fig. 5 Energy Dispersive Spectroscopy (EDS) spectrum of LSMO and LSMNO prepared by heat treated at 1500 °C for 24 h, shown as a plot of X-ray counts versus energy. Energy peaks corresponding to various elements in the sample are indicated

was no loss of any integral component after Ni substitution treatment. The appearance of the characteristic line of the Si element is due to the glass holder of the samples. The ratio of silicon and oxygen produced by the glass holder for samples was corrected and deleted from the device measurements, which depends on the atomic ratio of each element in SiO_2.

Table 3 presents three methods for measuring the proportions of the elements in the LSMO and LSMNO samples. The first method is to calculate the atomic ratios of the elements in a theoretical way, and the second method is done according to the characteristic lines in the spectrum of the EDX device. However, the third method is to calculate the ratio of the elements as the ratio of the atomic weight in the compound while keeping the stoichiometric chemical weight of the compound constant. The obtained results show that the ratio La/Sr is changed when adding nickel. This is due to the fact that the process is accompanied by amourphoucity increase which leads to the irregular atomic concentration. Especially, we see excess of oxygen on the surface.

3.3 Study of magnetization versus magnetic field

To evidence the effect of Ni addition on the LSMO perovskites, we will briefly report the valence of Ni when substituting Mn for large variety of manganites. In the case $La_{0.7}Pb0.3Mn_{1-x}Ni_xO_3$ in Full Ni concentration range (x = 0–0.5), XPS results confirm Ni^{2+} ionic nature. Similarly, via an EPR study of Ni-doped LaCaMnO Perovskite, Rubinstein [50] et al. found that Nickel exist as Ni^{2+} ions when replacing Mn. Same conclusion is also evidenced in the case of $La_{0.67}Sr_{0.33}Mn_{1-x}Ni_xO_3$ for lower Ni concentrations ($x \leq 0.2$) by an XPS study [19]. In the same context [14], it is demonstrated via an XPS study of $La_{0.8-}Sr_{0.2}Mn_{1-x}Ni_xO_3$ that when substituting Ni by Mn, the ratio of Ni^{3+}/Ni^{2+} decreases greatly for lower Ni concentration and also ionic entities of Mn are only Mn^{3+} and Mn^{4+}. However, as explained in reference [13], when there are oxygen vacancies, due to the formation of imbalance in the atomic ratio between O and Mn atoms a new adaptive situation produces

Table 3 Quantitative elemental analysis of LSMO and LSMNO perovskite prepared at 1500 °C for 24 h

Element	LSMO			LSMON		
	Theoretical At %	Wt %	Atomic %	Theoretical At %	Wt %	Atomic %
O	23.903	53.825	60.612	23.858	77.085	65.958
Mn	27.357	16.607	19.824	24.576	5.754	19.369
Ni	–	–	–	2.917	0.274	0.869
Sr	34.906	20.313	15.205	34.840	11.383	6.785
La	13.834	9.255	4.359	13.808	5.504	7.018
Total	100.00	100.00	100.00	99.999	100.00	99.999

Mn^{2+} ions. According to our synthesis route when supposing that there are no oxygen vacancies, the above published results permit to conclude that the preponderant ionic species are Ni^{2+}, Mn^{3+}, and Mn^{4+}.

Figure 6 shows the magnetization versus magnetic field for both materials. It is noted that the magnetization starts to saturate approximately at a magnetic field 2.5 KPo with nearly 0.563 μB and 0.357 μB, respectively, for LSMO and LSMNO. Then, the magnetization slightly continues to increase giving rise to a long tail, where their values reach 0.610 μB and 0.376 μB for higher magnetic field of 10 KPo. The long tail of magnetization in both cases is due to the competition between the ferromagnetic and antiferromagnetic moments coupling as demonstrated in the case of $La_{0.7}Sr_{0.3}Mn_{1-x}Ni_xO_3$ [51]. Therefore, before adding Nickel, the most origin ferro–antiferro competition arises essentially from ferromagnetic Mn^{3+}/Mn^{4+} moment and the antiferromagnetic Mn^{3+}/Mn^{3+} (and/or Mn^{4+}/Mn^{4+}) moments. However, after nickel addition, the new ferromagnetic Mn^{4+}/Ni^{2+} moment would be created. At the same time additional positive exchange interactions between Ni^{2+}/Mn^{3+} and Ni^{2+}/Ni^{2+} [52] would be created. To support the magnetization decrease, we refer to the global neutrality of both materials according to the material composition, where the charge conservation can be checked from the general electronic formula: $La^{3+}{}_{0.2}Sr^{2+}{}_{0.8}(Mn^{3+}{}_{0.2-y}, Mn^{4+}{}_{0.8-x+y})\ Ni_x{}^{2+}O_3{}^{2-}$. Indeed, in the case of the reference material $(La^{3+}{}_{0.2}Sr^{2+}{}_{0.8}(Mn^{3+}{}_{0.2}, Mn^{4+}{}_{0.8})O_3{}^{2-})$, both ionic entities Mn^{3+} and Mn^{4+} can contribute to the ferromagnetic coupling. However, when nickel is added at $x = 0.1(y = 2x)$ $(La^{3+}{}_{0.2}Sr^{2+}{}_{0.8}(Mn^{4+}{}_{0.9})\ Ni_{0.1}{}^{2+}O_3{}^{2-}$, only Mn^{4+} ions can exist, giving rise to the suppression of the Mn^{3+}/Mn^{4+} moment known as ferromagnetic components [52]. Therefore, the initial ferromagnetic moment (Mn^{3+}/Mn^{4+}) is replaced by Mn^{4+}/Ni^{2+} moment. The suppression of antiferromagnetic Mn^{3+}/Mn^{3+} moment is accompanied by the appearance of both Ni^{2+}/Mn^{3+} and Ni^{2+}/Ni^{2+} moments. Based on these results and according to the lower Ni concentration, the magnetization might be decreased. It is also reported that the decrease of magnetization saturation is related to a large grain boundary volume present in nano-crystalline influencing the number of atoms in ordered states [53].

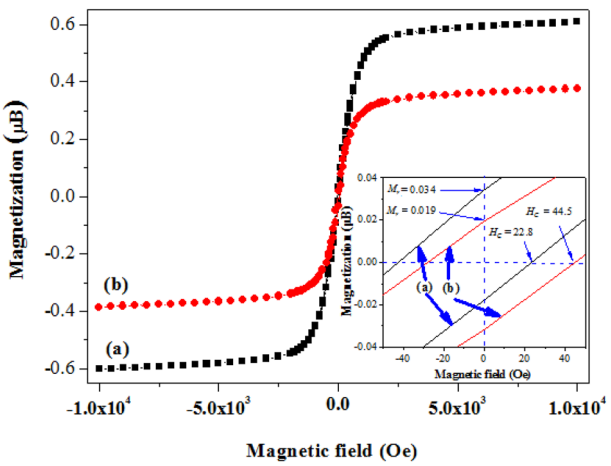

Fig. 6 The magnetization versus magnetic field for LSMO (**a**) and for LSMNO (**b**). The onset represents their hysteresis loop plot, respectively

The inset of Fig. 6 displays a hysteresis loop plot, which shows the remanent magnetization values M_r = 0.034 μB and 0.019 μB, respectively, for LSMO and LSMNO. Their corresponding coercive fields are approximately 22.8 Oe and 44.5 Oe. Therefore, the weak fraction of Ni substituting Mn induces the increase of coercive field and a net decrease of remanent magnetization. However, compared to other perovskites [25], H_c remains very weak, supporting their use as memory device. According to previous study [53, 54], the remanent magnetization depends on its saturation value. However, some other parameters lead to the variation of M_r and H_c, such as texture, nano-crystallites size, anisotropy, and phases present in the material. In our case, anisotropy caused by grain size decrease and the increase of amorphousity caused by Ni^{2+} cations lead to the magnetic moment arrangement and consequently the increase of coercivity.

3.4 Conductance analysis

The variation of the conductance G with frequency from 10^2 Hz to 5 MHZ in the temperature ranging from 300 to 420 K is shown in Fig. 7a and b, respectively, for LSMO and LSMNO samples. At lower frequency (less than 10^5 Hz), the conductance is approximately constant and correspond to the long range translational motion of ions [55]. In this frequency range, dominated by d_c conductance, the electric field cannot affect the hopping conduction mechanism. For both cases, the G_{dc} values (plateau) increase with temperature rising, indicating that the

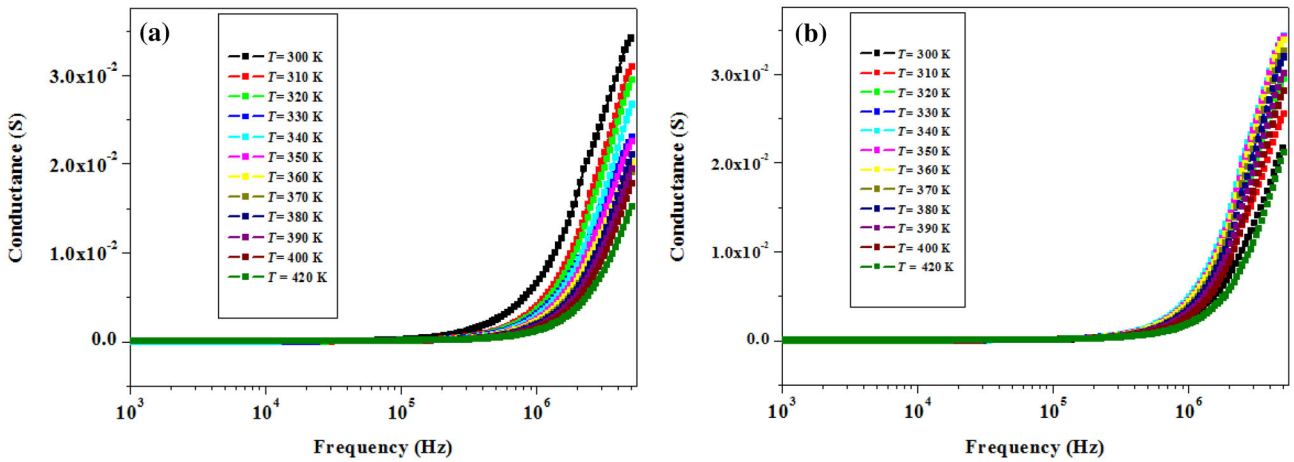

Fig. 7 Dependence of conductance with frequency in the temperature range 300–420 K for both LSMO (**a**) and LSMNO (**b**)

process is thermally activated where the mobile ion can hop successfully to its nearest vacant site. However, at higher frequencies the conductance increase sharply with frequency and correspond to the G_{ac}. In the full frequency range, the evolution of the conductance can be written as the single power Jonscher law [56]:

$$G(\omega) = G_{dc} + G_{ac} = G_{dc} + A\omega^{n} \tag{7}$$

In this expression, A represents the pre-exponential factor that determinates polarazability and n is a frequency factor, providing information degree of interaction between mobile carriers and lattices [57, 58]. The fitting data relative in all measurement temperatures are summarized in Table 4.

From these results, and based on continuous increase of G_{dc} in the full temperature range, we present the Arrhenius plot of the G_{dc} (T) according to (Eq. 8) in Fig. 8. In this equation, G_0 is the pre-exponential factor, E_a is the activation energy, K_B is the Boltzman constant, and T is the temperature. The activation energies required to activate the mobile charge carriers in both cases are calculated from the linear fit. In the case of LSMO, the activation energy until temperature range is 164 meV. However, in the case LSMNO, two temperature ranges are selected ($T < 400$ K) and ($T > 400$ K). Their typical corresponding activation energies are, respectively, 65 meV and 322 meV. We think that both energies are attributed to grain and grain size contributions. The obtained values of activation energies are in good agreement with other perovskites-type ferroelectric oxides [59].

$$G_{dc}(T) = G_0 \exp\left(-\frac{E_a}{k_B T}\right) \tag{8}$$

In all cases, the G_{dc} is assisted by trapping of polaron in the potential well of height E_a. When temperature gets higher, one side of the well will be lowered, allowing polarons jumping into the nearest neighboring site. This thermal process leads to the conductivity exponential rise, confirming thermally activated conduction.

Figures 9a and b illustrate, respectively, the evolution of frequency factor n as a function of temperature for both LSMO and LSMNO perovskites and the fitting parameters at the temperature of 420 K.

The temperature dependence of the frequency factor n permits to give specification of the G_{ac} conduction mechanisms [58]. As shown in Fig. 9a, the frequency factor in both cases is higher than 1 and shows a different variation. Based on the literature, the values of this factor can be either less or higher than 1, depending on the material nature. When n reaches values greater than 1, it is proposed [60] that the charge carriers undergo a motion encompassing localized hopping between neighboring sites and if n is less than 1, the motion involves a translational motion with a sudden hopping. Moreover, it has been recently reported [61] that ($n > 1$) means a motion of mobile charge carriers from site to site with tunneling effect as proposed by Gilory et al. [62]. In our case, for the LSMO, the n value shows globally a monotonic increase with temperature supporting the non-overlapping small polaron tunneling (NSPT) model for conductivity. However, in the case of LSMNO, the frequency factor n decreases until

Table 4 Fitting parameter of $G(\omega)$ according to Eq. 7

T (K)	Nickel content (x)	G_{dc} (10^{-5}) (S)	A (10^{-12}) (Si)	n	R^2
300	0.0	1.372	723.910	1.030	0.990
	0.1	0.855	5.252	1.286	0.996
310	0.0	1.785	224.790	1.224	0.991
	0.1	0.941	14.572	1.237	0.994
320	0.0	2.088	11.522	1.260	0.992
	0.1	0.9736	37.960	1.191	0.992
330	0.0	2.430	2.314	1.20574	0.991
	0.1	1.017	63.53	1.167	0.989
340	0.0	2.963	3.027	1.330	0.994
	0.1	1.119	68.140	1.168	0.986
350	0.0	3.402	3.8434	1.307	0.994
	0.1	1.137	36.050	1.204	0.987
360	0.0	3.856	3.852	1.300	0.994
	0.1	1.189	27.490	1.219	0.988
370	0.0	4.324	1.870	1.339	0.995
	0.1	1.263	14.507	1.254	0.9892
380	0.0	5.164	0.3120	1.447	0.997
	0.1	1.427	8.729	1.281	0.990
390	0.0	5.988	0.170	1.477	0.997
	0.1	1.5158	5.075	1.309	0.991
400	0.0	6.906	0.098989	1.5032	0.998
	0.1	1.7131	2.010	1.358	0.993
420	0.0	8.959	0.047	1.536	0.998
	0.1	2.676	0.2941	1.450	0.998

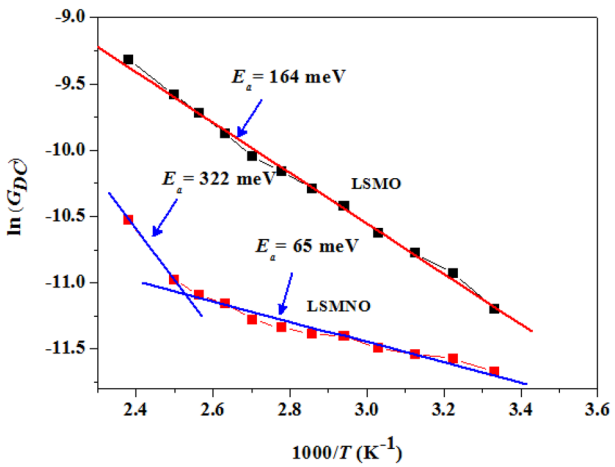

Fig. 8 Arrhenius plot of the $G_{dc}(T)$ in the temperature range 300–420 K: (■): Experimental and (—): Linear fit for both LSMO and LSMNO

reaching a minimum and then increases with rising temperature, matching well with the overlapping large polaron tunneling (OLPT) model [58]. Therefore, the interaction between individual charges and lattice distortion couldn't give overlapping in the case of LSMO. However, adding Nickel leads to give a higher spatial extension of the polaron wells by comparison to the interatomic distances, giving rise to the overlapping of two neighboring sites.

4 Conclusion

Perovskite oxide LSMO and LSMNO powders were successfully prepared by the standard solid-state reaction method in order to carry out the effect of lower Nickel substituted Mn on structural, magnetic, and conductive properties. EDX experimental results are in good accordance with those obtained theoretically, supporting the full integral reaction of all standard elements. From FESEM results, both materials contain agglomerations of nanoparticles constituted by grains and grain boundaries, with further reduced particle size when adding Ni element. Whereas X-ray analyses show that both materials crystallize in single-phase rhombohedral structure with 3RC group, Ni adding leads to some structural modifications such as the nano-crystallite size decrease and the increase of the amorphoucity. Lattice parameters and internal micro-strain are

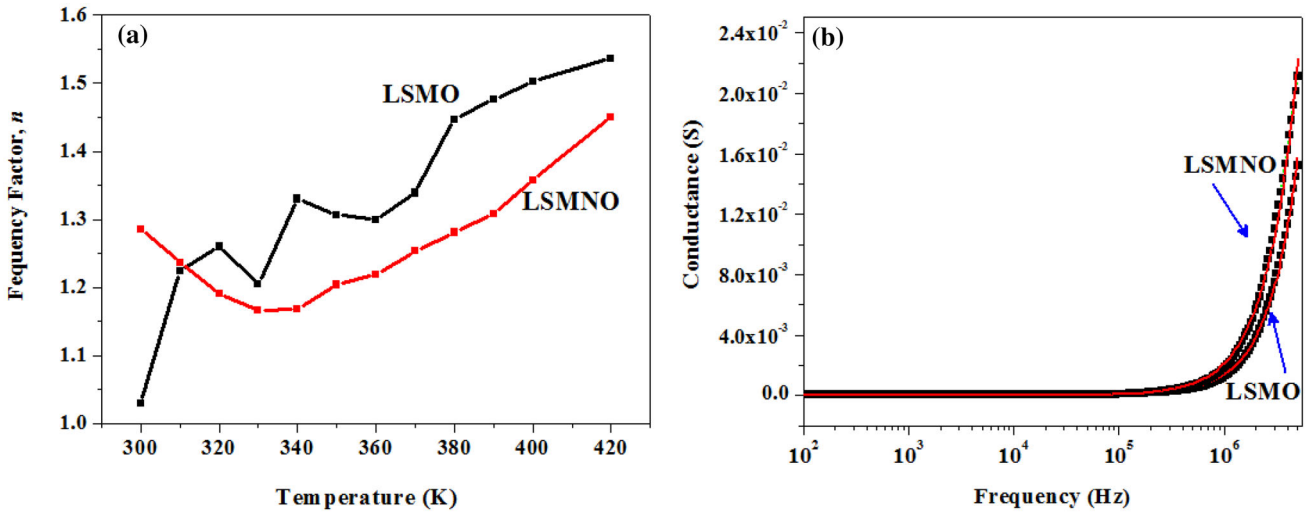

Fig. 9 **a** Frequency dependence of the factor (n) and **b** illustration of the fitting parameters at the temperature of 420 K for LSMO and LMSNO: (■) Experimental, (—) Fit using Eq. 7

consequently increased. Furthermore, from magnetic measurements, we support the existence of Nickel as Ni^{2+} replacing Mn^{3+} with approximately same radius ions which lead to reduce the saturation and remanent magnetizations and nearly twice value of the coercive field. Both ferromagnetic and antiferromagnetic moments coupling are present; however, Ni addition leads to the suppression of the Mn^{3+}/Mn^{4+} moment known as ferromagnetic components. Moreover, from conductance measurements, the lower frequency direct conductivity is thermally activated for which the activation energy deceases from 164 to 65 meV after Nickel addition. However, at higher frequencies, the conduction is assisted by non-overlapping small polaron tunneling (NSPT) model for LSMO and, the overlapping large polaron tunneling (OLPT) model for LSMNO. Nickel addition leads, therefore, to reducing the wall height and gives the resulting polaron a more spatial extension exceeding the interatomic distances.

References

1. L.W. Martin, Y.-H. Chu, R. Ramesh, Advances in the growth and characterization of magnetic, ferroelectric, and multiferroic oxide thin films. Mater. Sci. Eng. R Rep. **68**, 89 (2010). https://doi.org/10.1016/j.mser.2010.03.001
2. M.A. Subramanian, B.H. Toby, A.P. Ramirez, W.J. Marshall, A.W. Sleight, G.H. Kwe, Colossal magnetoresistance without Mn^{3+}/Mn^{4+} double exchange in the stoichiometric pyrochlore $TI_2Mn_2O_7$. Science **273**, 81 (1996). https://doi.org/10.1126/science.273.5271.81
3. M. Baibich, J. Broto, A. Fert, F. Nguyen Van Dau, F. Petroff, P. Etienne, G. Creuzet, A. Friederich, J. Chazelas, Giant magnetoresistance of (001)Fe/(001)Cr magnetic superlattices. J. Phys. Rev. Lett. **61**, 2472 (1988). https://doi.org/10.1103/PhysRevLett.61.2472
4. L. Balcells, R. Enrich, J. Mora, A. Calleja, J. Fontcuberta, Manganese perovskites: thick-film based position sensors fabrication. Appl. Phys. Lett. **69**, 1486 (1996). https://doi.org/10.1063/1.116916
5. S. Jin, T. Tiefel, M. McCormack, R. Fastnacht, R. Ramesh, L.H. Chen, Thousandfold, change in resistivity in magnetoresistive La-Ca-Mn-O films. Science **264**, 413 (1994). https://doi.org/10.1126/science.264.5157.413
6. W. Xia, Z. Pei, K. Leng, X. Zhu, Research progress in rare earth-doped perovskite manganite oxide nanostructures. Nanoscale Res. Lett. **15**, 9 (2020). https://doi.org/10.1186/s11671-019-3243-0
7. M. Egilmez, K. Chow, J. Jung, Anisotropic magnetoresistance in perovskite manganites. Mod. Phys. Lett. B. **25**, 697 (2011). https://doi.org/10.1142/S0217984911026176
8. G. George, S.L. Jackson, C.Q. Luo, D. Fang, D. Luo, D. Hu, J. Wen, Z. Luo, Effect of doping on the performance of high-crystalline $SrMnO_3$ perovskite nanofibers as a supercapacitor electrode. Ceram Int **44**, 21982 (2018). https://doi.org/10.1016/j.ceramint.2018.08.313
9. R. Bindu, K. Maiti, R. Rawat, S. Khalid, Electronic and structural transition in $La_{0.2}Sr_{0.8}MnO_3$. Appl. Phys. Lett. **92**, 121906 (2008). https://doi.org/10.1063/1.2898885
10. C. Doroftei, L. Leontie, Nanocrystalline $SrMnO_3$ perovskite prepared by sol–gel self-combustion method for sensor

applications. J. Sol-Gel Sci. Technol **97**, 146 (2021). https://doi.org/10.1007/s10971-020-05419-4

11. A. Kumar, M. Kumar, R.P. Singh, P.K. Singh, Opto-electronic, magnetic, thermodynamic and thermoelectric properties of cubic perovskite $SrMnO_3$: a first principle based spin polarized calculation. Solid State Commun. **324**, 114139 (2021). https://doi.org/10.1016/j.ssc.2020.114139
12. G.H. Jonker, J.H. Van Santen, Ferromagnetic compounds of manganese with perovskite structure. Physica **16**, 337 (1950). https://doi.org/10.1016/0031-8914(50)90033-4
13. J. Zhao, C. Liu, J. Li, R. Wu, J. Wang, H. Qian, H. Guo, J. Li, K. Ibrahim, Oxygen vacancy induced electronic structure variation in the $La_{0.2}Sr_{0.8}MnO_3$ thin film. AIP Adv. **9**, 055208 (2019). https://doi.org/10.1063/1.5088738
14. Z. Wang, Y. You, J. Yuan, Y.X. Yin, Y.T. Li, S. Xin, D. Zhang, Nickel-doped $La_{0.8}Sr_{0.2}Mn_{1-x}Ni_xO_3$ nanoparticles containing abundant oxygen vacancies as an optimized bifunctional catalyst for oxygen cathode in rechargeable lithium-air batteries. ACS Appl. Mater. Interfaces **8**, 6520 (2016). https://doi.org/10.1021/acsami.6b00296
15. E. Oumezzine, S. Hcini, E.-K. Hlil, E. Dhahri, M. Oumezzine, Effect of Ni-doping on structural, magnetic and magnetocaloric properties of $La_{0.6}Pr_{0.1}Ba_{0.3}Mn_{1-x}Ni_xO_3$ nanocrystalline manganites synthesized by Pechini sol–gel method. J. Alloy. Compd. **615**, 553 (2014). https://doi.org/10.1016/j.jallcom.2014.07.001
16. C.P. Reshmi, S.S. Pillai, K.G. Suresh, M.R. Va, Room temperature magnetocaloric properties of Ni substituted $La_{0.67}Sr_{0.33}MnO_3$. Solid State Sci. **19**, 130 (2013). https://doi.org/10.1016/j.solidstatesciences.2013.02.019Ge
17. B.D. Cullity, S.R. Stock, *Elements of X-Ray Diffraction*, 3rd edn. (Education Limited, London, Pearson, 2014), pp. 102–104
18. A.A.S. Akl, A.S. Hassanien, Microstructure and crystal imperfections of nanosized CdS_xSe_{1-x} thermally evaporated thin films. Superlatt Microstr. **85**, 67 (2015). https://doi.org/10.1016/j.spmi.2015.05.011
19. Z.H. Wang, J.W. Cai, B.G. Shen, X. Chen, W.S. Zhan, Exchange interaction, spin cluster and transport behaviour in perovskites $La_{0.67}Sr_{0.33}(Mn_{1-x}Ni_x)O_3$ ($x \leq 0.2$). J. Phys. Condens. Matter. **12**, 601 (2000). https://doi.org/10.1088/0953-8984/12/5/308
20. S. Kuharuangrong, Effects of Ni on the electrical conductivity and microstructure of $La_{0.82}Sr_{0.16}MnO_3$. Ceram. Int. **30**, 273 (2004). https://doi.org/10.1016/S0272-8842(03)00099-3
21. T. Ishihara, J.A. Kilner, M. Honda, Y. Takita, Oxygen surface exchange and diffusion in the new perovskite oxide ion conductor $LaGaO_3$. J. Am. Chem. Soc. **119**, 2747 (1997). https://doi.org/10.1021/ja964128l
22. S. Pala, E. Bose, B.K. Chaudhuri, H.D. Yang, S. Neeleshwar, Y.Y. Chen, Effect of Ni doping in rare-earth manganite $La_{0.7}Pb_{0.3}Mn_{1-x}Ni_xO_3$ (x=0.0–0.5). J. Magn. Magn. Mater. **293**, 872 (2005). https://doi.org/10.1016/j.jmmm.2004.12.005
23. A. Hammouche, E.J.L. Schouler, M. Henault, Electrical and thermal properties of Sr doped lanthanum manganites. Solid State Ion. (1988). https://doi.org/10.1016/0167-2738(88)90358-X
24. A.A. Akl, S.A. Mahmoud, S.M. Al-Shomar, A.S. Hassanien, Improving microstructural properties and minimizing crystal imperfections of nanocrystalline Cu_2O thin films of different solution molarities for solar cell applications. Mater. Sci. Semicond. Process. **74**, 183 (2018). https://doi.org/10.1016/j.mssp.2017.10.007
25. N. Hamdaoui, Y. Azizian-Kalandaragh, M. Khlifi, L. Beji, Structural, magnetic and dielectric properties of $Ni_{0.6}Mg_{0.4}Fe_2O_4$ ferromagnetic ferrite prepared by sol-gel method. Ceram. Int. **45**, 16458 (2019). https://doi.org/10.1016/j.ceramint.2019.05.177
26. F. Gaâbel, M. Khlif, N. Hamdaoui, L. Beji, K. Taibi, J. Dhahri, Microstructural, structural and dielectric analysis of Ni-doped $CaCu_3Ti_4O_{12}$ ceramic with low dielectric loss. J. Mater. Sci. Mater. Electron. **30**, 14823 (2019). https://doi.org/10.1007/s10854-019-01886-w
27. S.M. Salili, A. Ataie, M.R. Barati, Z. Sadighi, Characterization of mechano-thermally synthesized Curie temperature-adjusted $La_{0.8}Sr_{0.2}MnO_3$ nanoparticles coated with (3-aminopropyl) triethoxysilane. Mater. Charact. **106**, 78 (2015). https://doi.org/10.1016/j.matchar.2015.05.025
28. A. Peterlin, Molecular model of drawing polyethylene and polypropylene, Molecular model of drawing polyethylene and polypropylene. J. Mater Sci. **6**, 490 (1971). https://doi.org/10.1007/BF00550305
29. P.B. Bowden, R.J. Young, Deformation mechanisms in crystalline polymers. J. Mater Sci. **9**, 2034 (1974). https://doi.org/10.1007/BF00540553
30. A. Silambarasu, A. Manikandan, K. Balakrishnan, Room-temperature superparamagnetism and enhanced photocatalytic activity of magnetically reusable spinel $ZnFe_2O_4$ nanocatalysts. J. Supercond. Nov. Magn. **30**, 2631 (2017). https://doi.org/10.1007/s10948-017-4061-1
31. A. Manikandan, E. Hema, M. Durka, K. Seevakan, T. Alagesan, S.A. Antony, Room temperature ferromagnetism of magnetically recyclable photocatalyst of $Cu_{1-x}Mn_xFe_2O_4$-TiO_2 ($0.0 \leq x \leq 0.5$) nanocomposites. J. Supercond. Nov. Magn. **28**, 1783 (2015). https://doi.org/10.1007/s10948-014-2945-x
32. T. Dippong, O. Cadar, E.A. Levei, I.G. Deac, F. Goga, G. Borodi, L.B. Tudoran, Influence of polyol structure and molecular weight on the shape and properties of

$Ni_{0.5}Co_{0.5}Fe_2O_4$ nanoparticles obtained by sol-gel synthesis. Ceram. Int. **45**, 7458 (2019). https://doi.org/10.1016/j.ceramint.2019.01.037

33. J.M. Haudin, in: Plastic Deformation of Amorphous and Semi-crystalline Materials, ed. by B. Escaig and C. G'Sell (Les Editions de Physique, Les Ulis, France, 1982), p. 291–311.
34. L. Lin, A.S. Argon, Structure and plastic deformation of polyethylene. J. Mater. Sci. **29**, 294 (1994). https://doi.org/10.1007/BF01162485
35. J. Jia, D. Raabe. Crystallinity and crystallographic texture in isotactic polypropylene during deformation and heating. (ArXivLabs, 2008), http://arxiv.org/abs/0811.2412. Accessed 14 Nov 2008.
36. H. Klug, L. Alexander, *X-Ray Diffraction Procedures for Poly-Crystalline and Amorphous Materials*, 2nd edn. (Wiley, New York, 1974), pp. 136–142
37. A. Weidinger, P.H. Hermans, On the determination of the crystalline fraction of isotactic polypropylene from x-ray diffraction. Macromol. Chem. Phys. **50**, 98 (1961). https://doi.org/10.1002/macp.1961.020500107
38. A. Alaa, Akl, Microstructure and electrical properties of iron oxide thin films deposited by spray pyrolysis. Appl. Surf. Sci. **221**, 319 (2004). https://doi.org/10.1016/S0169-4332(03)00951-6
39. J. Zhang, J. Liu, Q. Peng, X. Wang, Y. Li, Nearly monodisperse Cu_2O and CuO nanospheres: preparation and applications for sensitive gas sensors. Chem. Mater. **18**, 867 (2006). https://doi.org/10.1021/cm052256f
40. Z. Zhang, C. Zhong, Y. Deng, L. Liu, Y. Wu, W. Hu, The manufacture of porous cuprous oxide film with photocatalytic properties *via* an electrochemical–chemical combination method. RSC Adv. **3**, 6763 (2013). https://doi.org/10.1039/C3RA40855H
41. S.M. Al-Shomar, M.A.Y. Barakat, S.A. Mahmoud, A.A. Akl, Microstructure, crystal imperfections and ultrasonic studies of sprayed nanosized Cu_2-xS_xO and $Cu_{2-y}Cr_yO$ thin films. Dig. J. Nanomater. Biostructures **13**, 885 (2018)
42. S. Eisermann, A. Kronenberger, A. Laufer, J. Bieber, G. Haas, S. Lautenschlager, G. Homm, P.J. Klar, B.K. Meyer, Copper oxide thin films by chemical vapor deposition: synthesis, characterization and electrical properties. Phys. Status Solidi A **209**, 531 (2011). https://doi.org/10.1002/pssa.201127493
43. A.O. Musa, T. Akomolafe, M.J. Carter, Production of cuprous oxide, a solar cell material, by thermal oxidation and a study of its physical and electrical properties. Sol. Energy Mater. Sol. Cells **51**, 305 (1998). https://doi.org/10.1016/S0927-0248(97)00233-X
44. A.A.S. Akl, M. Elhadi, Estimation of crystallite size, lattice parameter, internal strain and crystal impurification of nanocrystalline $Al_3Ni_{20}B_x$ alloy by Williamson-Hall method. J. of Ovonic Res. **16**, 323 (2020)
45. J.I. Langford, A.J.C. Wilson, Scherrer after sixty years: a survey and some new results in the determination of crystallite size. J. Appl. Cryst. **11**, 102 (1978). https://doi.org/10.1107/S0021889878012844
46. H. Song, W. Kim, S.-J. Kwon, Magnetic and electronic properties of transition metal substituted perovskite manganites $La_{0.7}Ca_{0.3}Mn_{0.95}X_{0.05}O_3$ (X=Fe Co, Ni). J. Appl. Phys. **89**, 3398 (2001). https://doi.org/10.1063/1.1350417
47. O. Toulemonde, F. Suder, A. Barnabe, A. Maignan, C. Martin, B. Raveau, Charge states of transition metal in "Cr, Co and Ni" doped $Ln_{0.5}Ca_{0.5}MnO_3$ CMR manganites. Eur. Phys. J. B **4**, 159 (1998). https://doi.org/10.1007/s100510050364
48. A.E.-M.A. Mohamed, B. Hernando, A.M. Ahmed, Magnetic, magnetocaloric and thermoelectric properties of nickel doped manganites. J. Alloy. Compd. **692**, 381 (2017). https://doi.org/10.1016/j.jallcom.2016.09.050
49. N. Hamdaoui, Y. Azizian-Kalandaragh, M. Khlifi, L. Beji, Cd-doping effect on morphologic, structural, magnetic and electrical properties of $Ni_{0.6-x}Cd_xMg_{0.4}Fe_2O_4$ spinel ferrite ($0 \leq x \leq 0.4$). J. Alloy. Compd. **803**, 964 (2019). https://doi.org/10.1016/j.jallcom.2019.06.339
50. M. Rubinstein, D.J. Gillespie, J.E. Snyder, T.M. Tritt, Effects of Gd Co, and Ni doping in $La_{2/3}Ca_{1/3}MnO_3$: resistivity, thermopower, and paramagnetic resonance. Phys. Rev. B **56**, 5412 (1997). https://doi.org/10.1103/PhysRevB.56.5412
51. J.W. Feng, L. Hwang, Ferromagnetic cluster behaviors and magnetoresistance in Ni-doped $LaSrMnO_3$ systems. Appl. phys. Lett. **75**(1592), 1592–1594 (1999). https://doi.org/10.1063/1.124764
52. O. Toulemonde, F. Studer, B. Raveau, Magnetic interactions studies of Co and Ni-doped manganites using soft XMCD. Solid State Commun. **118**, 107 (2001). https://doi.org/10.1016/S0038-1098(01)00020-5
53. M. Desai, S. Prasad, N. Venkataramani, I. Samajdar, A.K. Nigam, Anomalous variation of coercivity with annealing in nanocrystalline NiZn ferrite films. J. Appl. Phys. **91**, 592 (2002). https://doi.org/10.1063/1.1447504
54. V.M. Kalita, A.A.F. Lozenko, S.M. Ryabchenko, A.A. Timopheeev, R.A. Trotsenko, Magnetic properties of $La_{0.7}$-$Sr_{0.3}MnO_3$ nanopowders. Low Temp. Phys. **34**, 436 (2008). https://doi.org/10.1063/1.2920124
55. W. Li, R.W. Schwartz, Ac conductivity relaxation processes in $CaCu_3Ti_4O_{12}$ ceramics: grain boundary and domain boundary effects. Appl. Phys. Lett. **89**, 242906 (2006). https://doi.org/10.1063/1.2405382
56. A.K. Jonscher, The 'universal' dielectric response. Nature **267**, 673 (1977). https://doi.org/10.1038/267673a0

57. K.M. Sangwan, N. Ahlawat, S. Rani, S. Rani, R.S. Kundu, Influence of Mn doping on electrical conductivity of lead free $BaZrTiO_3$ perovskite ceramic. Ceram. Int. **44**, 10315 (2018). https://doi.org/10.1016/j.ceramint.2018.03.039
58. F. Gaâbel, M. Khlifi, N. Hamdaoui, K. Taibi, J. Dhahri, Conduction mechanisms study in $CaCu_{2.8}Ni_{0.2}Ti_4O_{12}$ ceramics sintered at different temperatures. J. Alloy. Compd. **828**, 154373 (2020). https://doi.org/10.1016/j.jallcom.2020.154373
59. M. Sindhu, N. Ahlawat, S. Sanghi, R. Kumari, A. Agarwal, Crystal structure refinement and investigation of electrically heterogeneous microstructure of single phased Sr substituted $BaTiO_3$ Ceramics. J. Alloy. Compd. **575**, 109 (2013). https://doi.org/10.1016/j.jallcom.2013.04.026
60. K. Funke, Jump relaxation in solid electrolytes. Prog. Solid State Chem. **22**, 111 (1993). https://doi.org/10.1016/0079-6786(93)90002-9
61. A. Dhahri, E. Dhahri, E.K. Hlil, Electrical conductivity and dielectric behaviour of nanocrystalline $La_{0.6}Gd_{0.1}Sr_{0.3}Mn_{0.75}Si_{0.25}O_3$. RSC Adv. **8**, 9103 (2018). https://doi.org/10.1039/C8RA00037A
62. K.S. Gilroy, W.A. Phillips, An asymmetric double-well potential model for structural relaxation processes in amorphous materials. Philos. Mag. Lett. **43**, 735 (1981). https://doi.org/10.1080/01418638108222343